

Valleytronics on the Surface of Topological Crystalline Insulator: Elliptic Dichroism and Valley-Selective Optical Pumping

Motohiko Ezawa

Department of Applied Physics, University of Tokyo, Hongo 7-3-1, 113-8656, Japan

The low-energy theory of the surface of the topological crystalline insulator (TCI) is characterized by four Dirac cones anisotropic into the x and y directions. Recent experiments have shown that the band gap can be introduced in these Dirac cones by crystal distortion by applying strain to the crystal structure. The TCI surface provides us with a new way to valleytronics when gaps are given to Dirac cones. Indeed the system has the Chern number and three valley-Chern numbers. We investigate the optical absorption on the TCI surface. It shows a strong elliptic dichroism though the four Dirac cones have the same chiralities. Namely, it is found that the absorptions of the right- and left-polarized light are different, depending on the sign of mass and the location of the Dirac cones, owing to the anisotropy of the Dirac cone. By measuring this elliptic dichroism it is possible to determine the anisotropy of a Dirac cone experimentally.

I. INTRODUCTION

Valleytronics is a promising candidate of the next generation electronics¹⁻⁷. It is a technology of manipulating the degree of freedom to which inequivalent degenerate state an electron belongs near the Fermi level. The main target of valleytronics is the honeycomb lattice system such as graphene. Indeed, the honeycomb structure is an ideal play ground of valleytronics since it has two inequivalent Dirac cones or *valleys*. A key progress in valleytronics is valley-selective optical pumping^{4,5,8-12}. By applying circular polarized light in a gapped Dirac system, we can selectively excite electrons in one valley based on the property that two valleys have opposite chiralities. It is known as the circular dichroism. Valley-selective pumping has been observed¹³⁻¹⁸ in the transition-metal dichalcogenides such as MoS₂, where there exists a direct gap between the conduction and valence bands for Dirac fermions.

However, the valleytronics is not restricted to the honeycomb system. Recently, the topological crystalline insulator (TCI) attracts much attention due to its experimental realizations¹⁹⁻²¹ in Pb_{1-x}Sn_xTe. It is a topological insulator protected by the mirror symmetry^{22,23}. The remarkable properties of the TCI is that there emerge four topological protected surface Dirac cones, as has been observed in the angle-resolved photoelectron spectroscopy (ARPES) experiment¹⁹⁻²¹. The appearance of several topologically protected Dirac cones enables us to use the TCI as the basic material for the valleytronics. Recent experiments²⁴ show that the band gap can be introduced in the surface Dirac cones by crystal distortion by applying strain to the crystal structure.

In this paper, we investigate the optical absorption of the TCI surface. The key properties of surface Dirac cones are that all of them have the same chirality but that each of them has a particular anisotropy. Based on the anisotropy, we can selectively excite electrons in different valley by the elliptically polarized light. This is a new type of dichroism different from the circular dichroism. We call it an *elliptic dichroism*. We propose an experimental method to determine the anisotropy of the velocities and the band gap of Dirac cones with the use of elliptic dichroism. Our finding will open a new way of the valleytronics based on the TCI.

The present paper is composed as follows. In Section II, we introduce the low-energy Hamiltonians H_X and H_Y valid near the X and Y points for the [001] surface, which are related by the C_4 discrete rotation symmetry. The Hamiltonian contains the pseudospin degree of freedom representing the cation and the anion. The X (Y) point is separated into a pair of the Λ_X and Λ'_X (Λ_Y and Λ'_Y) points due to the spin-pseudospin mixing. We then derive the four low-energy Hamiltonians describing four Dirac cones at the $\Lambda_X, \Lambda'_X, \Lambda_Y$ and Λ'_Y points. They have in general Dirac electrons with different masses m_X, m'_X, m_Y and m'_Y . In Section III, we study the spin and pseudospin structures around the X and Y points. In Section IV, we analyze the Chern number for each Dirac cone. It is simply given by $\pm\frac{1}{2}$ depending on the sign of the Dirac mass. Since there are four Dirac cones, there arise the Chern number and three valley-Chern numbers. The Chern number is a genuine topological number, while valley-Chern numbers are symmetry-protected topological numbers. When the mass is induced by the strain, the Chern number is zero because of the time-reversal symmetry. On the other hand, when the mass is induced by the exchange effect, the Chern number is ± 2 per surface. In Section V, we investigate optical absorption and elliptic dichroism by exciting massive Dirac electrons by the right or left elliptically polarized light. We show that the optical absorption is determined by the Chern number of each Dirac cone and that the elliptic dichroism occurs owing to the anisotropy of a Dirac cone. It is interesting that the elliptic dichroism is observable on the surface of the TCI with the Dirac mass being induced by the strain.

II. HAMILTONIAN

Recent ARPES experiments¹⁹⁻²¹ show that there are four Dirac cones at $\Lambda_X, \Lambda'_X, \Lambda_Y$ and Λ'_Y points in the [001] surface state of the TCI, whose band structure we show in Fig.1(a). They may be used as the valley degree of freedom. Two Dirac cones are present at the Λ_X and Λ'_X points near the X point but slightly away from the X point along the x axis in the momentum space. The other two Dirac cones are present at the Λ_Y and Λ'_Y points near the Y point along the y axis. It is notable that the Dirac cones reside at the mirror

symmetry invariant points along the ΓX and ΓY lines rather than at the time-reversal symmetry invariant X and Y points, implying that the protected symmetry is the mirror symmetry and not the time-reversal symmetry.

The Hamiltonian for the [001] surface states of the TCI near the Y point has been given in literature^{25–28} as

$$H_Y(\mathbf{k}) = v_2 k_x \sigma_y - v_1 k_y \sigma_x + n \tau_x + n' \sigma_x \tau_y + m \sigma_z. \quad (1)$$

The Hamiltonian near the X point is given by

$$H_X(\mathbf{k}) = v_1 k_x \sigma_y - v_2 k_y \sigma_x + n \tau_x + n' \sigma_y \tau_y + m \sigma_z, \quad (2)$$

as we shall soon see. Here, σ and τ are the Pauli matrixes for the spin and the pseudospin representing the cation-anion degree of freedom, respectively: n and n' describe the pseudospin mixing. We have set $\hbar = 1$ for simplicity. Typical values are $v_1 = 1.3\text{eV}$, $v_2 = 2.4\text{eV}$, $n = 70\text{meV}$ and $n' = 26\text{meV}$ ^{23,25}. The term $m \sigma_z$ represents the exchange magnetization with the exchange field m , and acts as the mass term. It may be regarded as the Zeeman term without external magnetic field. It may arise due to proximity coupling to a ferromagnet, as enhances the exchange interaction to align the spin direction. We show the band structure without and with this term in Fig.1(b) and (c), respectively.

The crystal structure of the $\text{Pb}_{1-x}\text{Sn}_x\text{Te}$ is a rocksalt structure. Accordingly, the [001] surface has the inverse C_4 discrete rotation symmetry such that

$$\sigma_x \mapsto \sigma_y, \quad \sigma_y \mapsto -\sigma_x \quad (3)$$

together with

$$k_x \mapsto k_y, \quad k_y \mapsto -k_x. \quad (4)$$

Using this transformation, we obtain Eq.(2) valid near the X point from Eq.(1) valid near the Y point. Note that the velocities into the x and y directions are different at the Y point from those at the X point, as is a manifestation of the four-fold rotation symmetry.

It follows from (2) that the energy spectrum is given by

$$E(\mathbf{k}) = \pm \sqrt{f \pm 2\sqrt{g}} \quad (5)$$

in the vicinity of the X point with

$$f = n^2 + n'^2 + v_1^2 k_x^2 + v_2^2 k_y^2 + m^2, \quad (6a)$$

$$g = (n^2 + n'^2) v_1^2 k_x^2 + n^2 v_2^2 k_y^2 + n^2 m^2. \quad (6b)$$

The band structure is shown in Fig.1. The gap closes at the two points $(k_x, k_y) = (\pm\Lambda, 0)$ with $\Lambda = \sqrt{n^2 + n'^2}/v_1$ without the mass term ($m = 0$). They are the Λ_X and Λ'_X points.

An intriguing feature of the TCI surface is the mass acquisition^{23,29} by crystal distortion, as has been observed in recent experiments²⁴. They are $\pm\Delta m_X$ and $\pm\Delta m_Y$ at the Λ_X (Λ'_X) and Λ_Y (Λ'_Y) points, respectively. Combining the mass m due to the exchange effect, the mass reads²⁹

$$\begin{aligned} m_X &= m + \Delta m_X, & m'_X &= m - \Delta m_X, \\ m_Y &= m + \Delta m_Y, & m'_Y &= m - \Delta m_Y \end{aligned} \quad (7)$$

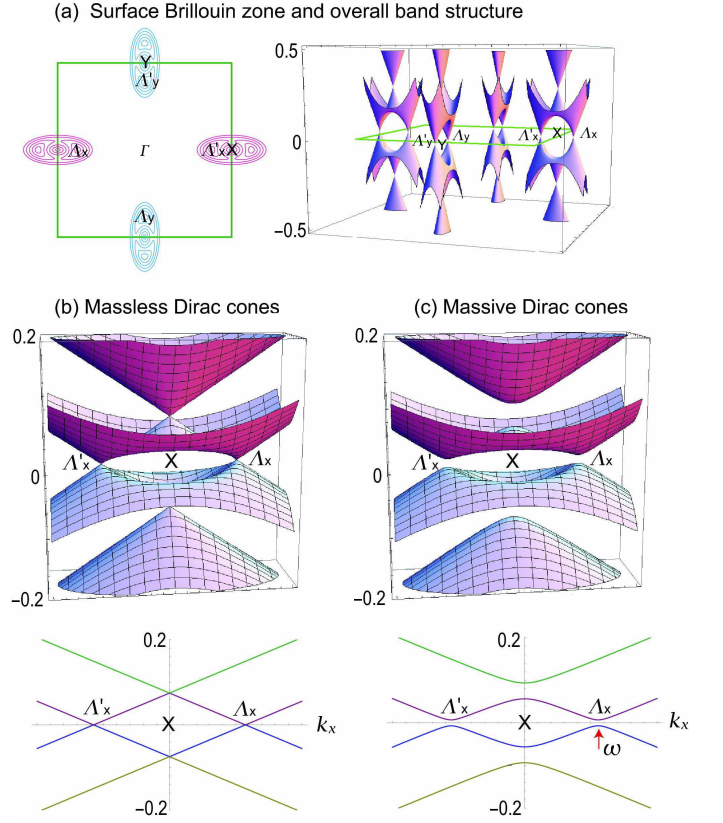


FIG. 1: (Color online) (a) Surface Brillouin zone centered at the Γ point and bounded by the X and Y points. There are low-energy Dirac cones at the Λ_X , Λ'_X , Λ_Y , Λ'_Y points, and high-energy Dirac cones at the X and Y points. (b) Detailed band structure in the vicinity of the X point. Two low-energy Dirac cones are formed at the Λ_X and Λ'_X points. (c) The gaps open when the mass term is present.

at each Dirac point. There might be other mechanisms to generate the mass. The mass term is necessary for the valley-selective optical absorption to occur. However the following analysis is independent of detailed origins of the mass term.

By linearizing the band structure around the Λ_X point, we obtain the two-component low-energy Hamiltonian for massive Dirac fermions^{25,27},

$$H_{\Lambda_X}(\tilde{\mathbf{k}}) = \tilde{v}_1 \tilde{k}_x \sigma_y - \tilde{v}_2 \tilde{k}_y \sigma_x + \tilde{m}_X \sigma_z, \quad (8)$$

which describes physics near the Fermi level, where $\tilde{k}_x = k_x - \Lambda$ and $\tilde{k}_y = k_y$, with the renormalized velocity,

$$\tilde{v}_1 = v_1 \sqrt{1 - \frac{m_X^2 n^2 (n^2 + n'^2)}{[(n^2 + n'^2)^2 + m_X^2 n^2]^{3/2}}} \simeq v_1, \quad (9a)$$

$$\begin{aligned} \tilde{v}_2 &= v_2 \sqrt{1 - \frac{n^2}{\sqrt{(n^2 + n'^2)^2 + m_X^2 n^2}}} \\ &\simeq v_2 n' / \sqrt{n^2 + n'^2} = 0.84\text{eV}, \end{aligned} \quad (9b)$$

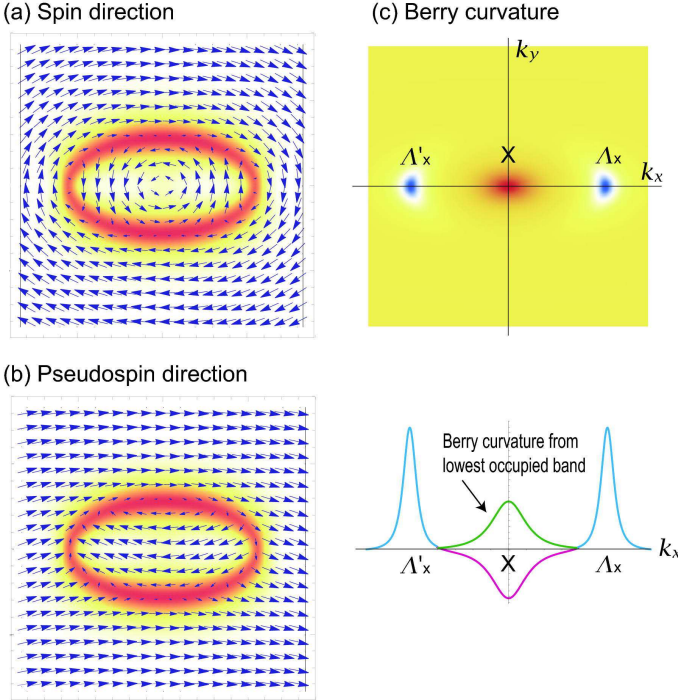


FIG. 2: (Color online) (a) Spin direction of the TCI surface in the vicinity of the X point. The red oval indicates the region where the magnitude of spin is quite small. The spin directions are opposite inside and outside the oval. The spin rotation is clockwise (anticlockwise) in the low-energy (high-energy) Dirac cones at the Λ_X and Λ'_X points (the X point). (b) Pseudospin direction of the TCI surface in the vicinity of the X point. The red oval indicates the region where the magnitude of pseudospin is quite small. The pseudospin directions are opposite inside and outside the oval. (c) Berry curvature of the highest occupied band. It has a sharp peak (red) at the X point and sharp peaks (blue) at the Λ_X and Λ'_X points. The Chern number contribution from the Berry curvature at the X point is exactly cancelled out by the one (green) from the Dirac cone in the lowest occupied band at the X point.

and the renormalized mass,

$$\tilde{m}_X = \text{sgn}(m_X) \sqrt{m_X^2 + 2n^2 + 2n'^2 - 2\sqrt{(n^2 + n'^2)^2 + m_X^2 n^2}}. \quad (10)$$

The energy spectrum reads

$$E_{\Lambda_X} = \pm \sqrt{\tilde{v}_1^2 \tilde{k}_x^2 + \tilde{v}_2^2 \tilde{k}_y^2 + \tilde{m}_X^2}. \quad (11)$$

The linearized Hamiltonian around the Λ'_X point has precisely the same expression as (8) except that \tilde{m}_X is replaced by \tilde{m}'_X . In the same way we have the low-energy Hamiltonian around the Λ_Y point,

$$H_{\Lambda_Y}(\tilde{\mathbf{k}}) = \tilde{v}_2 \tilde{k}_x \sigma_y - \tilde{v}_1 \tilde{k}_y \sigma_x + \tilde{m}_Y \sigma_z, \quad (12)$$

where $\tilde{k}_x = k_x$ and $\tilde{k}_y = k_y - \Lambda$, and the similar one around the Λ'_Y point.

III. SPIN DIRECTION

We illustrate the expectation value of the spin $\langle \mathbf{s} \rangle = \langle \psi | \mathbf{s} | \psi \rangle$ in the vicinity of the X point in Fig.2(a). There is one up-pointing vortex with anti-clockwise vorticity at the X point, and there are two down-pointing vortices with clockwise vorticity at the Λ_X and Λ'_X points^{28,30,31}. They describe the spin directions of electrons in one Dirac cone at the X point, and two Dirac cones at the Λ_X and Λ'_X points in Fig.1.

This structure is understood as follows. Let us assume $n = 0$ and $n' = 0$ in Eq.(2). Then the two Dirac cones in the conduction and valence bands touch each other at the Fermi level. The effect of the term $n\tau_x$ is to shift these Dirac cones to intersect one another, forming an intersection oval. (It is an oval and not a circle since $v_1 \neq v_2$.) These two Dirac cones have opposite chiralities, which leads to the opposite spin rotations inside and outside the oval. We now switch on n' . Then the level crossing turns into the level anticrossing with the resulting band structure as in Fig.1(a), where Dirac cones emerge at the Λ_X and Λ'_X points. The spin rotates around each Dirac cone. The magnitude of spin, $s^2 = s_x^2 + s_y^2 + s_z^2$, is found to be quite small around the oval [Fig.2(a)]. We clearly see the directions of the spin rotation are identical in the four valleys at Λ_X , Λ'_X , Λ_Y and Λ'_Y , which manifests the identical chirality of the four low-energy Dirac cones. On the other hand, the spin rotation in the two high-energy Dirac cones at the X and Y points is opposite to the one in the low-energy Dirac cones. The spin direction has been observed by means of spin-resolved ARPES^{20,30}.

We have also illustrated the expectation value of the pseudospin in the vicinity of the X point in Fig.2(b). The pseudospin vector points the x -direction when $n' = 0$ in Eq.(2), since then τ_x is a good quantum number. The pseudospin direction is inverted at the oval, which is the interception of the two Dirac cones. When $n' \neq 0$, the magnitude of the pseudospin, $\mathbf{t}^2 = t_x^2 + t_y^2 + t_z^2$, becomes quite small also around the oval.

The fact that the magnitudes of the pure spin and pseudospin are quite small around the oval leads to a strong entanglement of the spin and pseudospin there, as we now argue. The Hamiltonian is described by the 4×4 matrix, which results in the $SU(4)$ group structure of the system. The $SU(4)$ group is decomposed into the pure spin and pseudospin parts and the spin-pseudospin entangled part. The generators of the pure spin (pseudospin) part are given by σ_i (τ_i) with $i = x, y, z$. On the other hand, those of the spin-pseudospin entangled part are given by $\sigma_i \tau_j$ with $i, j = x, y, z$, which compose the $SU(2) \otimes SU(2)$ group. The magnitude of the $SU(4)$ spin is a constant and takes the same value everywhere. Hence, the fact that the pure spin and pseudospin components become quite small means that the spin-pseudospin entangled components such as $\sigma_z \tau_y$ and $\sigma_y \tau_z$ become large. The results implies a rich topological structure in the $SU(4)$ space.

IV. CHERN NUMBER AND VALLEY-CHERN NUMBER

The Chern number is obtained by the integration over the whole Brillouin zone. We illustrate the Berry curvature $F(\mathbf{k})$ of the highest unoccupied state in Fig.2(c). The Berry curvature is found to exhibit sharp peaks at the vortex centers of the spin rotation, which correspond to the tips of the Dirac cones, and become zero away from them. Hence, the Chern number is given by the sum of the contributions from individual Dirac cones. Note that the Berry curvature at the X point is exactly canceled out by the one from the other occupied band, and does not contribute to the Chern number.

In the vicinity of the Λ_X point, we obtain an analytic form for the Berry curvature $F_X(\mathbf{k})$ by using the low-energy Hamiltonian (8),

$$F_X(\mathbf{k}) = \frac{\tilde{m}_X \tilde{v}_1 \tilde{v}_2}{(\tilde{v}_1^2 k_x^2 + \tilde{v}_2^2 k_y^2 + \tilde{m}_X^2)^{3/2}}. \quad (13)$$

The Chern number is explicitly calculated as

$$C_X = \frac{1}{2\pi} \int F(\mathbf{k}) d\mathbf{k} = \frac{1}{2} \text{sgn}(\tilde{m}_X) = \frac{1}{2} \text{sgn}(m_X), \quad (14)$$

which is associated with the Dirac cone at the Λ_X point. The similar formulas are derived for C'_X , C_Y and C'_Y with the use of m'_X , m_Y and m'_Y for the Dirac cones at the Λ'_X , Λ_Y and Λ'_Y points, respectively.

At low energy there are four Dirac Hamiltonians such as (8) and (12), each of which describes a Dirac cone possessing a definite Chern number depending on the sign of the Dirac mass. Hence there are four Chern numbers. The genuine Chern number is their sum,

$$C = C_X + C'_X + C_Y + C'_Y. \quad (15)$$

This is a genuine topological number.

In addition, there are three valley-Chern numbers³², which we may take as

$$C_1 = C_X + C'_X - C_Y - C'_Y, \quad (16a)$$

$$C_2 = C_X - C'_X + C_Y - C'_Y, \quad (16b)$$

$$C_3 = C_X - C'_X - C_Y + C'_Y. \quad (16c)$$

They are symmetry-protected topological numbers. The relevant symmetry is the valley symmetry, which is the permutation symmetry of Dirac valleys. This is a good symmetry near the Fermi level, since the system is described by four Dirac Hamiltonians independent each other. However, at higher energy, the system is described by the tight-binding Hamiltonian, containing inter-valley hoppings, where there is no valley symmetry.

If we treat the four masses independently there are 16 topological states indexed by (C, C_1, C_2, C_3) . However, when there are constraints on them, they read as follows:

(1) When we apply only the exchange field ($\Delta m_X = \Delta m_Y = 0$), we find $\pm(2, 0, 0, 0)$ with $C_X = C_Y = C'_X = C'_Y$.

(2) When we apply only the strain ($m = 0$), we find $\pm(0, 0, 2, 0)$ with $C_X = C_Y = -C'_X = -C'_Y$ for

$\Delta m_X \Delta m_Y > 0$, and $\pm(0, 0, 0, 2)$ with $C_X = -C_Y = -C'_X = C'_Y$ for $\Delta m_X \Delta m_Y < 0$.

(3) When we apply both the exchange field and the strain to the crystal, we find $\pm(1, -1, 1, 1)$ for $\Delta m_X > m > 0$ and $m > \Delta m_Y > 0$.

There are some other cases depending on m , Δm_X and Δm_Y . We have found that the Chern number may take values 2, 1, 0, -1, -2. Even if it is zero, the state is topological with respect to the valley-Chern numbers.

V. OPTICAL ABSORPTION AND ELLIPTIC DICHOISM

An interesting experiment to probe and manipulate the valley degree of freedom is to employ the optical absorption^{4,5,8-10,12}. It is possible to excite massive Dirac electrons by the right or left circularly polarized light, known as circular dichroism. Originally, circular dichroism is proposed in honeycomb systems, where the velocities of the Dirac cones are isotropic. On the other hand they are anisotropic in the TCI surface. This leads to the elliptic dichroism, where the optical absorptions are different between the right and left elliptically polarized lights. Furthermore, the optical absorptions depend crucially on the sign of the Dirac mass.

A. Kubo formula

We explore optical inter-band transitions from the state $|u_v(\tilde{\mathbf{k}})\rangle$ in the valence band to the state $|u_c(\tilde{\mathbf{k}})\rangle$ in the conduction band. The fundamental transition is a transition from the highest occupied band to the lowest unoccupied band (Fig.1). We inject a beam of elliptical polarized light onto the TCI surface. The corresponding electromagnetic potential is given by $\mathbf{A}(t) = (A_x \sin \omega t, A_y \cos \omega t)$. The electromagnetic potential is introduced into the Hamiltonian by way of the minimal substitution, that is, by replacing the momentum \tilde{k}_i with the covariant momentum $P_i \equiv \tilde{k}_i + eA_i$. The resultant Hamiltonian simply reads $H(A) = H + \mathcal{P}_x A_x + \mathcal{P}_y A_y$, with

$$\mathcal{P}_x = \frac{\partial H}{\partial \tilde{k}_x}, \quad \mathcal{P}_y = \frac{\partial H}{\partial \tilde{k}_y}, \quad (17)$$

in the linear response theory.

The optical absorption is governed by the Fermi golden rule. Namely, the imaginary part of the dielectric function arises due to inter-band absorption, and is given by the Kubo formula. In the case of elliptical polarized light it reads⁴

$$\varepsilon_\theta(\omega) = \frac{\pi e^2}{\varepsilon_0 m_e^2 \omega^2} \sum_i \int_{BZ} \frac{d\tilde{\mathbf{k}}}{(2\pi)^2} f(\tilde{\mathbf{k}}) \left| P_\theta(\tilde{\mathbf{k}}) \right|^2 \times \delta \left[E_c(\tilde{\mathbf{k}}) - E_v(\tilde{\mathbf{k}}) - \omega \right], \quad (18)$$

with the use of the optical matrix element $P_\theta(\tilde{\mathbf{k}})$, where $E_c(\tilde{\mathbf{k}})$ and $E_v(\tilde{\mathbf{k}})$ are the energies of the conduction and valence

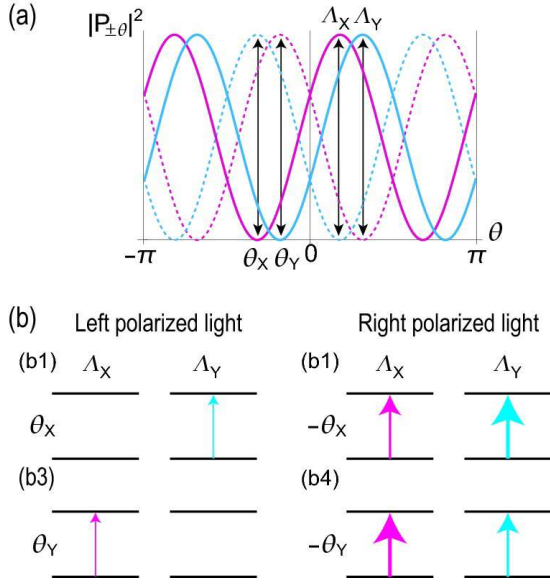


FIG. 3: (Color online) (a) Optical matrix element $|P_{\pm\theta}|^2$ at the Λ_X and Λ_Y points with various ellipticity θ [Eq.(26)]. Red (blue) solid curves are optical absorption $|P_\theta|^2$ at the X (Y) point, and dotted curves are for $|P_{-\theta}|^2$. (b) Illustration of optical absorption $|P_\theta|^2$ at (b1) $\theta = \theta_X$, (b2) $\theta = -\theta_X$, (b3) $\theta = \theta_Y$, (b4) $\theta = -\theta_Y$. The magnitude of arrows indicates the magnitude of optical absorption. We have assumed that all four masses have positive values.

bands, while $f(\tilde{\mathbf{k}})$ is the Fermi distribution function. The coupling strength with optical fields is given by the optical matrix element between the initial and final states in the photoemission process^{4,5,8,9},

$$P_i(\tilde{\mathbf{k}}) \equiv m_0 \left\langle u_c(\tilde{\mathbf{k}}) \left| \frac{\partial H}{\partial k_i} \right| u_v(\tilde{\mathbf{k}}) \right\rangle, \quad (19)$$

which is the interband matrix element of the canonical momentum operator. The optical matrix element for elliptically polarized light is

$$P_\theta(\tilde{\mathbf{k}}) = P_x(\tilde{\mathbf{k}}) \cos \theta + iP_y(\tilde{\mathbf{k}}) \sin \theta, \quad (20)$$

where θ is the ellipticity of the injected beam. We call it the right polarized light for $0 < \theta < \pi$ and the left one for $-\pi < \theta < 0$.

B. Optical absorption at the Dirac point

We first investigate optical interband transitions from the valence-band tops to the conduction band bottoms, i.e., at the Dirac point. By adjusting the energy of light to the band edge, namely, at $\tilde{\mathbf{k}} = 0$,

$$\omega = E_c(0) - E_v(0) = 2|\tilde{m}|, \quad (21)$$

we find

$$\varepsilon_\theta(2|\tilde{m}|) = \frac{\pi e^2}{4\varepsilon_0 m_e^2 \tilde{m}^2} |P_\theta(0)|^2 \quad (22)$$

at each Dirac point, where \tilde{m} can be any of \tilde{m}_X , \tilde{m}'_X , \tilde{m}_Y , \tilde{m}'_Y . It follows that $|P_\theta(0)|^2$ can be directly observed by optical absorption.

The wave functions $|u_v(\tilde{\mathbf{k}})\rangle$ and $|u_c(\tilde{\mathbf{k}})\rangle$ are obtained explicitly by diagonalizing Eq.(2), and we have

$$P_x(0) = \tilde{v}_1, \quad P_y(0) = -i\tilde{v}_2 \text{sgn}[m_X]. \quad (23)$$

It is possible to derive an explicit form of $|P_\theta^\pm(0)|^2_{\Lambda_X}$ at the Λ_X point for arbitrary ellipticity θ as

$$|P_\theta(0)|^2_{\Lambda_X} = m_0^2 (\tilde{v}_1 \cos \theta + \text{sgn}[m_X] \tilde{v}_2 \sin \theta)^2. \quad (24)$$

Similar formulas follow at the other Dirac points. By introducing

$$\tan \phi_X = \tilde{v}_1/\tilde{v}_2, \quad \tan \phi_Y = \tilde{v}_2/\tilde{v}_1, \quad (25)$$

we rewrite them as

$$|P_\theta(0)|^2_{\Lambda_X} = m_0^2 (\tilde{v}_1^2 + \tilde{v}_2^2) \sin^2(\phi_X + \text{sgn}[m_X] \theta), \quad (26a)$$

$$|P_\theta(0)|^2_{\Lambda'_X} = m_0^2 (\tilde{v}_1^2 + \tilde{v}_2^2) \sin^2(\phi_X + \text{sgn}[m'_X] \theta), \quad (26b)$$

and

$$|P_\theta(0)|^2_{\Lambda_Y} = m_0^2 (\tilde{v}_1^2 + \tilde{v}_2^2) \sin^2(\phi_Y + \text{sgn}[m_Y] \theta), \quad (26c)$$

$$|P_\theta(0)|^2_{\Lambda'_Y} = m_0^2 (\tilde{v}_1^2 + \tilde{v}_2^2) \sin^2(\phi_Y + \text{sgn}[m'_Y] \theta). \quad (26d)$$

We note that

$$\phi_X = 0.317\pi, \quad \phi_Y = 0.183\pi \quad (27)$$

for $v_1 = 1.3\text{eV}$, $v_2 = 2.4\text{eV}$, and that

$$\phi_X + \phi_Y = \frac{\pi}{2} \pmod{\pi}. \quad (28)$$

There are four functions with the same amplitude in general: See Fig.3(a). The function (red solid curve) involving $|\sin(\phi_X + \theta)|^2$ is the main one. The function (blue solid curve) involving $|\sin(\phi_Y + \theta)|^2$ is constructed by sifting it so that (28) holds. The other two functions (dotted curves) are constructed by changing $\theta \rightarrow -\theta$.

For instance, when all masses are positive such as in the case of the exchange effect, it follows that $|P_\theta(0)|^2_{\Lambda_X} = |P_\theta(0)|^2_{\Lambda'_X}$, as is shown in the red solid lines in Fig.3(a). It also follows that $|P_\theta(0)|^2_{\Lambda_Y} = |P_\theta(0)|^2_{\Lambda'_Y}$, as is shown in blue solid curves in Fig.3(a).

For instance, when $m_X m'_X < 0$ and $m_Y m'_Y < 0$ such as in the case of the strain effect, it follows that $|P_\theta(0)|^2_{\Lambda_X} = |P_{-\theta}(0)|^2_{\Lambda'_X}$ and $|P_\theta(0)|^2_{\Lambda_Y} = |P_{-\theta}(0)|^2_{\Lambda'_Y}$. Thus, if $m_X > 0$ and $m_Y > 0$, they are described by the same solid curves at the Λ_X and Λ_Y points but by the dotted curves at the Λ'_X and Λ'_Y points in Fig.3(a).

A perfect elliptic dichroism is a phenomenon that only one-handed elliptically polarized light is absorbed. It occurs at $\theta = -\phi_X$ for the function $|\sin(\phi_X + \theta)|^2$. At the same point the function $|\sin(\phi_Y + \theta)|^2$ takes the maximum value. More

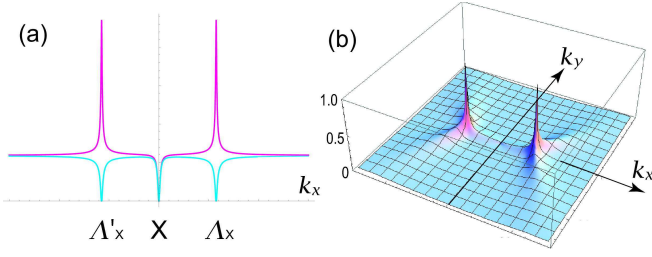


FIG. 4: (Color online) (a) Optical matrix element $|P_{\theta_X}(\tilde{\mathbf{k}})|^2$ (red curve) and $|P_{-\theta_X}(\tilde{\mathbf{k}})|^2$ (blue curve) along the \tilde{k}_x axis, (b) $\tilde{\mathbf{k}}$ -resolved optical polarization $\eta(\tilde{\mathbf{k}})$. It has two sharp peaks at the Λ_X and Λ'_X points. We have taken $\tilde{m}_X = \tilde{m}_Y = 2\text{meV}$.

explicitly they occur as $\theta = \theta_X$ at the Λ_X point and so on, with

$$\begin{aligned} \theta_X &= -\text{sgn}[m_X] \phi_X, & \theta'_X &= -\text{sgn}[m'_X] \phi_X, \\ \theta_Y &= -\text{sgn}[m_Y] \phi_Y, & \theta'_Y &= -\text{sgn}[m'_Y] \phi_Y. \end{aligned} \quad (29)$$

We give an example in Fig.3(a) when all the masses are positive, where $\theta'_X = \theta_X$ and $\theta'_Y = \theta_Y$.

We have studied analytically the optical matrix element $|P_\theta(\tilde{\mathbf{k}})|$ at the Dirac point. Next we investigate it away from the Dirac point. An analytic solution of the optical matrix element of right and left elliptically polarized light $|P_\theta(\tilde{\mathbf{k}})|^2$ is obtained from Eq.(2). However, the expression is very complicated. We show the result in Fig.4 at $\theta = \theta_X$, which shows the low-energy Dirac theory captures the essential features. There are sharp peaks in optical absorption near the Λ_X (Λ'_X) points. Fig.4(a) shows the optical matrix element $|P_{\theta_X}(\tilde{\mathbf{k}})|^2$ and $|P_{-\theta_X}(\tilde{\mathbf{k}})|^2$ along the \tilde{k}_x axis. We clearly see the difference between the right and left polarized lights at the Λ_X (Λ'_X) point. There is large optical absorption in right polarized light, while no optical absorption in left polarized light. This is a dichroism caused by elliptically polarized light, and the key feature of the elliptic dichroism.

C. Optical absorption away from the Dirac point

We proceed to derive the analytic expression of $|P_\theta(\tilde{\mathbf{k}})|$ away from the Λ_X point with the use of the the low-energy Hamiltonian (8) in (19). It is straightforward to find that

$$P_x(\tilde{\mathbf{k}}) = \tilde{v}_1 \frac{\tilde{v}_1 \tilde{k}_x \tilde{m}_X + i \tilde{v}_2 \tilde{k}_y \sqrt{\tilde{m}_X^2 + \tilde{v}_1^2 \tilde{k}_x^2 + \tilde{v}_2^2 \tilde{k}_y^2}}{\sqrt{\tilde{v}_1^2 \tilde{k}_x^2 + \tilde{v}_2^2 \tilde{k}_y^2} \sqrt{\tilde{m}_X^2 + \tilde{v}_1^2 \tilde{k}_x^2 + \tilde{v}_2^2 \tilde{k}_y^2}}, \quad (30a)$$

$$P_y(\tilde{\mathbf{k}}) = \tilde{v}_2 \frac{\tilde{v}_2 \tilde{k}_y \tilde{m}_X - i \tilde{v}_1 \tilde{k}_x \sqrt{\tilde{m}_X^2 + \tilde{v}_1^2 \tilde{k}_x^2 + \tilde{v}_2^2 \tilde{k}_y^2}}{\sqrt{\tilde{v}_1^2 \tilde{k}_x^2 + \tilde{v}_2^2 \tilde{k}_y^2} \sqrt{\tilde{m}_X^2 + \tilde{v}_1^2 \tilde{k}_x^2 + \tilde{v}_2^2 \tilde{k}_y^2}}, \quad (30b)$$

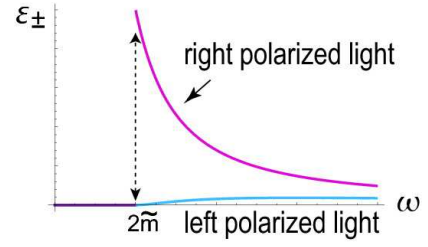


FIG. 5: (Color online) Imaginary part of dielectric function $\epsilon_{\pm}(\omega)$ due to interband absorptions at $\theta = \theta_X$: See Eq.(34). A clear difference is observed between the right and left polarized lights. There is almost no optical absorption for left polarized light for $\omega > 2\tilde{m}$. We have taken $\tilde{m} > 0$ for definiteness.

since $\mathcal{P}_x = \tilde{v}_1 \sigma_x$ and $\mathcal{P}_y = \tilde{v}_2 \sigma_y$. At $\theta = \theta_X$, it yields a simple form,

$$|P_{\theta_X}(\tilde{\mathbf{k}})|^2 = m_0^2 \tilde{v}_1 \tilde{v}_2 \frac{\left(\pm \tilde{m}_X + \sqrt{\tilde{m}_X^2 + \tilde{v}_1^2 \tilde{k}_x^2 + \tilde{v}_2^2 \tilde{k}_y^2} \right)^2}{\tilde{m}_X^2 + \tilde{v}_1^2 \tilde{k}_x^2 + \tilde{v}_2^2 \tilde{k}_y^2}. \quad (31)$$

We derive the same formula away from the Λ'_X point just replacing \tilde{m}_X with \tilde{m}'_X . Similar formulas are derived also with respect to the Λ_Y and Λ'_Y points.

Representing (31) in terms of the energy (11), we obtain

$$|P_\theta(\tilde{\mathbf{k}})|^2 = m_0^2 \tilde{v}_1 \tilde{v}_2 \frac{(\pm \tilde{m} + E_v(\tilde{\mathbf{k}}))^2}{[E_v(\tilde{\mathbf{k}})]^2}, \quad (32)$$

at $\theta = \theta_{X(Y)}$ with the use of $\tilde{m} = \tilde{m}_{X(Y)}$, and $\theta = \theta'_{X(Y)}$ with the use of $\tilde{m} = \tilde{m}'_{X(Y)}$, where we have used the relation $\varepsilon_v(\tilde{\mathbf{k}}) = -\varepsilon_c(\tilde{\mathbf{k}})$ required by the electron-hole symmetry of the energy spectrum.

We substitute (32) to (18), and use the density of state

$$\rho(E) = \frac{|E|}{2\pi \tilde{v}_1 \tilde{v}_2} \Theta(E - 2|\tilde{m}|) \quad (33)$$

with the step function $\Theta(x) = 1$ for $x > 0$ and $\Theta(x) = 0$ for $x < 0$, to find

$$\varepsilon_{\pm}(\omega) = \frac{e^2 m_0^2}{2\varepsilon_0 m_e^2 \omega} \frac{(\pm \tilde{m} + \omega/2)^2}{(\hbar\omega/2)^2} \Theta(\omega - 2|\tilde{m}|). \quad (34)$$

Hence there is no optical absorption for

$$\omega = \mp 2\tilde{m} > 0. \quad (35)$$

We show the optical absorption (34) in Fig.5. A clear difference is observed between the right- and left- polarized lights. There is almost no optical absorption for left polarized light for $\omega > 2|\tilde{m}|$. Here, \tilde{m} stands for any of \tilde{m}_X , \tilde{m}'_X , and \tilde{m}'_Y .

A perfect elliptic dichroism follows that $|P_{\theta_X}(0)|^2 = 0$ if $m_X > 0$, while $|P_{-\theta_X}(0)|^2 = 0$ if $m_X < 0$. The anisotropy of the Dirac cone is determined by measuring the ellipticity angle θ_X of the injected beam: See Fig.3. We would expect

$\theta_X = 0.317\pi$ as in (27). We can also determine the band gap by measuring the energy where the optical absorption becomes nonzero (34): See Fig.5. The role of the right- and left-polarized light is inverted when the sign of the mass term is negative. Thus we can determine the sign of the mass term by the elliptic dichroism even when the magnitude of the mass term is very small.

D. Optical polarization

We next investigate the k -resolved optical polarization $\eta_\theta(\tilde{\mathbf{k}})$, which is given by^{4,5,8,9}

$$\eta_\theta(\tilde{\mathbf{k}}) = \frac{|P_\theta(\tilde{\mathbf{k}})|^2 - |P_{-\theta}(\tilde{\mathbf{k}})|^2}{|P_\theta(\tilde{\mathbf{k}})|^2 + |P_{-\theta}(\tilde{\mathbf{k}})|^2}, \quad (36)$$

which we show in Fig.4(b). This quantity is the difference between the absorption of the left- and right-handed lights ($\pm\theta$), normalized by the total absorption, around the Λ_X point. Optical polarizations are perfectly polarized at the Λ_X and Λ'_X points ($\tilde{\mathbf{k}} = 0$). Namely, the selection rule holds exactly at the Λ_X and Λ'_X points. Then, $|\eta_\theta(\tilde{\mathbf{k}})|$ rapidly decreases to 0 as $|\tilde{\mathbf{k}}|$ increases.

E. Valley-selective optical pumping

An interesting valleytronics application of the elliptic dichroism would read as follows. Let us adjust the ellipticity of light at $\theta = \theta_X$ so that the optical absorption near the Λ_X point does not occur [Fig3(b1)]. Then the optical absorption

is not zero at the Λ_Y point. Namely, we can selectively excite electrons at the Λ_Y point by left polarized light. It is a valley-selective optical pumping. In the same way, by adjusting $\theta = \theta_Y$, we can selectively excite electrons at the Λ_X point by left polarized light [Fig3(b3)]. The valley-selective optical pumping is possible since the anisotropy of Dirac cones at Λ_X and Λ_Y points are different. If the Dirac cones were isotropic, we could not differentiate the Dirac cones at Λ_X and Λ_Y points since they have the same chirality. This will pave a new way to valleytronics in the TCI.

VI. CONCLUSIONS

We have investigated the optical absorption on the TCI surface when gaps are given to surface Dirac cones. First, the chiralities of all four Dirac cones are identical, which can be verified by studying the spin direction. Nevertheless, it is possible to make a selective excitation between the Λ_X (Λ'_X) point and the Λ_Y (Λ'_Y) point, because the Dirac cones are anisotropic, where $\tilde{v}_2/\tilde{v}_1 = 0.65$. Furthermore, it is also possible to make a selective excitation between the Λ_X and Λ'_X points when the Dirac masses \tilde{m}_X and \tilde{m}'_X have the opposite signs. Namely, by tuning the ellipticity of the polarized light, we can realize a perfect elliptic dichroism, where only electrons at one valley are excited. Our results will pave a new road toward valleytronics based on the TCI.

I am very much grateful to N. Nagaosa, Y. Ando, L. Fu and T. H. Hsieh for many helpful discussions on the subject. This work was supported in part by Grants-in-Aid for Scientific Research from the Ministry of Education, Science, Sports and Culture No. 22740196.

-
- ¹ A. Rycerz, J. Tworzydło, and C. W. J. Beenakker, *Nat. Phys.* **3**, 172 (2007).
² D. Xiao, W. Yao, and Q. Niu, *Phys. Rev. Lett.* **99**, 236809 (2007).
³ A. R. Akhmerov, C. W. J. Beenakker, *Phys. Rev. Lett.* **98**, 157003 (2007).
⁴ W. Yao, D. Xiao, and Q. Niu, *Phys. Rev. B* **77**, 235406 (2008).
⁵ D. Xiao, G.-B. Liu, W. Feng, X. Xu, and W. Yao, *Phys. Rev. Lett.* **108**, 196802 (2012).
⁶ M. Ezawa, *Phys. Rev. Lett.* **109**, 055502 (2012).
⁷ M. Ezawa, *Phys. Rev. B* **88**, 161406 (R) (2013).
⁸ X. Li, T. Cao, Q. Niu, J. Shi, and J. Feng, *PNAS* **110** (10) 3738 (2013).
⁹ M. Ezawa, *Phys. Rev. B* **86**, 161407(R) (2012).
¹⁰ L. Stille, C. J. Tabert, E. J. Nicol, *Phys. Rev. B* **86**, 195405 (2012).
¹¹ M. Ezawa, *Phys. Rev. B* **87**, 155415 (2013).
¹² Z. Li, J. P. Carbotte, *Phys. Rev. B*, **87**, 155416 (2013).
¹³ K. F. Mak, C. Lee, J. Hone, J. Shan, and T. F. Heinz, *Phys. Rev. Lett.* **105**, 136805 (2010).
¹⁴ A. Splendiani, L. Sun, Y. Zhang, T. Li, J. Kim, C.-Y. Chim, G. Galli, and F. Wang, *Nano Lett.* **10**, 1271 (2010).
¹⁵ H. Zeng, J. Dai, W. Yao, D. Xiao and X. Cui, *Nat. Nanotech.* **7**, 490 (2012).
¹⁶ T. Cao, G. Wang, W. Han, H. Ye, C. Zhu, J. Shi, Q. Niu, P. Tan, E. Wang, B. Liu and J. Feng *Nat. Com.* **3**, 887 (2012).
¹⁷ K. F. Mak, K. He, J. Shan and T. F. Heinz, *Nat. Nanotech.* **7**, 494 (2012).
¹⁸ S. Wu, J. Ross, G. Liu, G. Aivazian, A. Jones, Z. Fei, W. Zhu, D. Xiao, W. Yao, D. Cobden, X. Xu, *Nature Physics* **9**, 149 (2013).
¹⁹ Y. Tanaka, Z. Ren, T. Sato, K. Nakayama, S. Souma, T. Takahashi, K. Segawa and Y. Ando, *Nat. Phys.* **8**, 800 (2012).
²⁰ S.-Y. Xu, C. Li, N. Alidoust, M. Neupane, D. Qian, I. Belopolski, J.D. Denlinger, Y.J. Wang, H. Lin, L.A.Wray, G. Landolt, B. Slomski, J.H. Dil, A. Marcinkova, E. Morosan, Q. Gibson, R. Sankar, F.C. Chou, R. J. Cava, A. Bansil and M.Z. Hasan, *Nat. Com.* **3**, 1192 (2012).
²¹ P. Dziawa, B. J. Kowalski, K. Dybko, R. Buczko, A. Szczepakow, M. Szot, E. Lusakowska, T. Balasubramanian, B. M. Wojek, M. H. Berntsen, O. Tjernberg and T. Story, *Nat. Mat.* **11**, 1023 (2012).
²² L. Fu, *Phys. Rev. Lett.* **106**, 106802 (2011).
²³ T. H. Hsieh, H. Lin, J. Liu, W. Duan, A. Bansil and L. Fu, *Nat. Comm.* **3**, 982 (2012).
²⁴ Y. Okada, M. Serbyn, H. Lin, D. Walkup, W. Zhou, C. Dhital, M. Neupane, S. Xu, Y. J. Wang, R. Sankar, F. Chou, A. Bansil, M. Z. Hasan, S. D. Wilson, L. Fu, V. Madhavan, *Science* **341** 1496 (2013).
²⁵ J. Liu, W. Duan, L. Fu, *Phys. Rev. B* **88**, 241303(R) (2013).

- ²⁶ C. Fang, M. J. Gilbert, S.-Y. Xu, B. A. Bernevig, and M. Z. Hasan, Phys. Rev. B **88**, 125141 (2013)
- ²⁷ J. Liu, T. H. Hsieh, P. Wei, W. Duan, J. Moodera and L. Fu, Nat. Mat. **13** 178 (2014).
- ²⁸ Y. J Wang, W.-F. Tsai, H. Lin, S.-Y. Xu, M. Neupane, M. Z. Hasan, and A. Bansil, Phys. Rev. B **87** 235317 (2013)
- ²⁹ C. Fang, M. J. Gilbert, B. A. Bernevig, Phys. Rev. Lett. **112**, 046801 (2014)
- ³⁰ B. M. Wojek, R. Buczko, S. Safaei, P. Dziawa, J. Kowalski, M. H. Berntsen, T. Balasubramanian, M. Leandersson, Phys. Rev. B **87** 115106 (2013).
- ³¹ S. Safaei, P. Kacman, and R. Buczko, Phys. Rev. B **88** 045305 (2013)
- ³² M. Ezawa, Phys. Lett. A **378**, 1180 (2014)